The Wabar impact craters, Saudi Arabia, revisited

E. GNOS[1]*, B. A. HOFMANN[2], M. A. HALAWANI[3], Y. TARABULSI[3], M. HAKEEM[3],
M. AL SHANTI[3], N. D. GREBER[2,4], S. HOLM[5], C. ALWMARK[5],
R. C. GREENWOOD[6], and K. RAMSEYER[4]

[1]Natural History Museum of Geneva, 1, route de Malagnou, CP 6434, Geneva 6, 1205, Switzerland
[2]Natural History Museum Bern, Bernastrasse 15, Bern 3005, Switzerland
[3]Saudi Geological Survey, P.O. Box 54141, Jeddah 21514, Saudi Arabia
[4]Institute of Geological Sciences, University of Bern, Baltzerstrasse 1 + 3, Bern 3012, Switzerland
[5]Department of Geology, Lund University, Sölvegatan 12, Lund 223 62, Sweden
[6]Planetary and Space Sciences, The Open University, Milton Keynes MK7 6AA, UK
*Corresponding author. E-mail: edwin.gnos@ville-ge.ch

Abstract–The very young Wabar craters formed by impact of an iron meteorite and are known to the scientific community since 1933. We describe field observations made during a visit to the Wabar impact site, provide analytical data on the material collected, and combine these data with poorly known information discovered during the recovery of the largest meteorites. During our visit in March 2008, only two craters (Philby-B and 11 m) were visible; Philby-A was completely covered by sand. Mapping of the ejecta field showed that the outcrops are strongly changing over time. Combining information from different visitors with our own and satellite images, we estimate that the large seif dunes over the impact site migrate by approximately 1.0–2.0 m yr^{-1} southward. Shock lithification took place even at the smallest, 11 m crater, but planar fractures (PFs) and undecorated planar deformation features (PDFs), as well as coesite and stishovite, have only been found in shock-lithified material from the two larger craters. Shock-lithified dune sand material shows perfectly preserved sedimentary structures including cross-bedding and animal burrows as well as postimpact structures such as open fractures perpendicular to the bedding, slickensides, and radiating striation resembling shatter cones. The composition of all impact melt glasses can be explained as mixtures of aeolian sand and iron meteorite. We observed a partial decoupling of Fe and Ni in the black impact glass, probably due to partitioning of Ni into unoxidized metal droplets. The absence of a Ca-enriched component demonstrates that the craters did not penetrate the bedrock below the sand sheet, which has an estimated thickness of 20–30 m.

INTRODUCTION

The Kingdom of Saudi Arabia, the largest country on the Arabian peninsula, presently has only few documented meteorite finds and impact craters (see Earth Impact Database, http://www.passc.net). In March 2008, we undertook an investigation of the Wabar craters with the aim of investigating temporal changes in sand cover and studying the preservation state of the Wabar craters, which are located in an active dune field.

The Wabar craters, as plotted on the geological map by Bramkamp and Ramirez (1959), are located at 21°30.25′ N/50°28.30′ E (Fig. 1). They were first described by Philby (1933a, 1933b), who was shown their location by Bedouins. The local people believed that they were the remains of the destroyed city of Wabar (or Ubar; Philby 1933a), described in the Holy Qu'ran. This myth appears to be a consequence of the rounded shape of the craters and the ejecta rims resembled the broken walls of castles. In addition, the glasses found in the area were taken as evidence that a

Fig. 1. Overview map of the Arabian Peninsula showing the location of the Wabar (=Al Hadidah) impact craters in the Rub' al Khali (stippled line).

strong fire had destroyed the city. The Bedouins also knew that a large piece of iron (hadid), the size of a "camel hump," was lying in the vicinity of the glass. The use of the two names Wabar and Al Hadidah for the same locality caused considerable confusion among the early explorers of the area. Before Philby arrived at Wabar in 1932, the Bedouins warned him that the place was sometimes completely covered by sand and no sign of Wabar could then be detected. Although the large iron meteorite was completely covered by sand at the time that Philby explored the area, it was re-exposed in 1965 and collected on the 16th or 17th October 1965, by Jim Mandaville and an Aramco colleague. It was subsequently described by Abercrombie (1966). In this article, he also mentions that an Aramco exploration team found three craters at the Wabar site. The nicely ablated 2040 kg iron meteorite piece (Fig. 2a), 107 × 60 cm in size, is covered with fused sand on its frontal flight side. Mandaville also reported (Appendix S1) that their group found an additional large, 210 kg meteorite (Fig. 2b). The total mass of iron meteorite fragments recovered from the Wabar area since 1863 is estimated to be about 2.55 tons (Grady 2000). The two largest recovered iron fragments, the 2040 kg specimen (photos presented in Abercrombie 1966; Buchwald 1975; and Edgell 2006; Fig. 2a) and the 210 kg specimen (Fig. 2b), are at the Natural History Museum in Riyadh. The main masses of the other large recovered fragments, a 62 kg specimen (former Nejed II) and a 59.4 kg

specimen (former Nejed I), are held at the Field Museum in Chicago and the Natural History Museum in London, respectively. The 10.7 kg sample collected by Philby in 1932, as shown on page 174 in Philby (1933a), is now held at the Natural History Museum in London (Grady 2000).

Wabar is classified as a group IIIAB iron meteorite. Detailed analyses are provided in Buchwald (1975) and Mittlefehldt et al. (1992). An earlier analysis was listed in Spencer and Hey (1933), yielding 92 wt% Fe, 7.3 wt% Ni, with a quoted density of 7.66 g cm^{-3}. Because of the very low concentration of Fe and Ni in the sand dunes (Mittlefehldt et al. 1992), Wabar provided unequivocal evidence that impact glass can contain a considerable contribution from the impacting meteorite (e.g., Mittlefehldt et al. 1992).

The age of the impact craters was estimated by Storzer and Wagner (1977) at approximately 6400 yr, using fission tracks in impact melt droplets. Prescott et al. (2004) considered this age too old and redated impactite material with thermoluminescence (TL) dating methods at 290 ± 38 yr before present (corresponding to AD1714 ± 38) for the impact (ages ranging from 235 to 416 yr). Basurah (2003) correlated the Wabar impact event with the description, in two historic poems, of a bright fireball on September 1, 1704, observed in Tarim, Yemen (Fig. 1), 620 km SSW of Wabar. Reports that the fall occurred in 1863 are unsubstantiated, as discussed in Philby (1933a) and Prescott et al. (2004).

Here, we present additional geological data on the Wabar ejecta field obtained during fieldwork organized by the Saudi Geological Survey in March 2008. These new data are used as a basis for re-evaluating the results of earlier studies of the Wabar event.

SAMPLES AND ANALYTICAL METHODS

The coordinates of craters and separately fallen iron meteorite fragments (as reported in Table 1) are based on our own Global Positioning System measurements of the 11 m crater and the rim of crater Philby-B. Other coordinates were estimated relative to these positions using the crater map in Wynn (2002) and personal information obtained from Jim Mandaville (2008; Appendix S1). All analyzed samples were collected during our visit to the Wabar impact site, from 23rd to 25th March 2008. In addition to material from the impact site, we report data for a fulgurite (surface sand fused by lightning) collected in the vicinity of the impact craters at 21°29.926′ N, 50°28.223′ E, and on dune sand collected 6.3 km NW of Wabar at 21°32.262′ N, 50°25.410′ E.

Polished thin sections were used for petrographic, electron microprobe, cathodoluminescence, and U-stage

Fig. 2. Wabar impact site. a) Largest preserved, aerodynamically shaped and strongly grooved Wabar (iron IIIAB) meteorite fragment at its find locality after being overturned. This shape indicates a stable atmospheric flight (no tumbling of the object). Photo courtesy of Aramco World. b) 210 kg angular fragment collected by Jim Mandaville and a colleague from Aramco. Note the poorly visible regmaglypts on the front side. Photo by Jim Mandaville. c) Philby-B crater, as seen from top of seif dune (this study). The crater is almost completely filled up with sand; only small sections of the crater rim are visible. d) 11 m crater, as seen from top of seif dune in March 2008. Note that this crater was completely covered by the dune between 2009 and 2012.

Table 1. Coordinates of main craters and of the largest meteorite fragments.

Crater/meteorite	Latitude	Longitude	Impactor diameter (m)	Mass (t)
Philby-A (center)	21°30.28′	50°28.27′	5.3[a]	597[b]
Philby-B (center)	21°30.20′	50°28.36′	9.5[a]	3439[b]
11 m crater (center)	21°30.275′	50°28.295′	0.9[a]	2.9[b]
Camel Hump	21°30.00′#	50°28.27′#		2.04
Mandaville	21°29.89′#	50°28.35′#		0.21

[a]Based on estimates given in Wynn and Shoemaker (1998), assuming a factor of 12 (diameter/impactor size) for a soft target crater; # Jim Mandaville (personal communication 2008).

[b]Assuming spherical shape and using measured Wabar density of 7.66 g cm^{-3}.

studies. Rock fragments and powders were used for X-ray diffraction (XRD), X-ray fluorescence (XRF), inductively coupled optical emission spectroscopy (ICP-OES), inductively coupled mass spectrometry (ICP-MS), energy dispersive X-ray spectrometry (EDS), and oxygen isotope studies. Conventional gas counting techniques were used for radiocarbon dating of plant stems. Analytical details are given in Appendix S2.

THE WABAR IMPACT SITE

Location of Impact Craters and Large Iron Meteorites

The Wabar impact site, in Arabic "Al Hadidah" (=the iron; Figs. 1 and 2a), is completely enclosed by

the sand dunes of the Rub' al Khali (Empty Quarter). The closest outcrops of limestone bedrock visible on satellite imagery are 30 km to the NE (Ibrahima wells, elevation 155 m) and 90 km to the WNW (Bir Ash Shalfa, elevation 200 m). The wells of Umm al Hadid and Faraja, approximately 20 km NE of Wabar, also penetrated into the bedrock (Philby 1933a). The estimated bedrock elevation is 160–170 m at Wabar and the mean local elevation of the sand is 190 m (Google Earth elevation model). The thickness of the sand sheet at Wabar can be estimated to be at least 20–30 m based on the uniform gentle slope of the flat desert floor exposed in the larger area.

Three craters are present at the Wabar site (Fig. 3), Philby-A with a diameter of 64 m, Philby-B with a diameter of 116 m (Fig. 2c), and the "11 m crater" (Fig. 2d; Shoemaker and Wynn 1997). The depth of the partially sand-filled Philby-B crater was given by Philby (1933b) as 12.2 m. Spencer and Hey (1933) listed a width-to-depth ratio of 8, which would correspond to a depth of 14.5 m for Philby-B. According to Wynn (2002), Philby-B was completely covered by sand, as shown in an aerial photograph from 1961. The depth of Philby-B was 8 m in 1965 (estimate from James Mandaville in Shoemaker and Wynn 1997), a little over 1 m in 1990 (estimate from Jens Munthe in Shoemaker and Wynn 1997), 3 m in 1995 (Shoemaker and Wynn 1997), and 20–30 cm in March 2008 (only top of crater rim exposed; see Fig. 2c). None of the investigators had access to the crater floor. Shoemaker and Wynn (1997) and Wynn (2002) provided detailed maps of the ejecta exposures for 1995, when all three craters were visible.

The largest, 2040 kg Wabar IIIAB iron specimen (Fig. 2a) was found in 1863 and recovered in 1965 (Abercrombie 1966). The 210 kg, regmaglypt-covered piece (Fig. 2b) was recovered at the same time (often reported differently). Find coordinates based on information provided by Jim Mandaville (Appendix S1) are compiled in Table 1 and shown in Fig. 3. The find positions of the 62 kg, the 59.4 kg, and the 10.7 kg samples are unfortunately not known.

It is known that impact structures in sedimentary rocks are shallower than those in crystalline rocks (e.g., Grieve 1987). By using the Holsapple (1993) scaling method for dry sand, a 7.66 g cm^{-3} impactor density, impact angles between 0° and 45° relative to vertical and impact velocities of 5–25 km s^{-1}, crater depth estimates for Philby-B do not exceed 15 m. This is less than the estimated thickness of the dune sand sheet. That the craters are located entirely within the sand sheet is supported by the fact that the ejected material consists exclusively of shock-lithified dune sand and lacks limestone blocks.
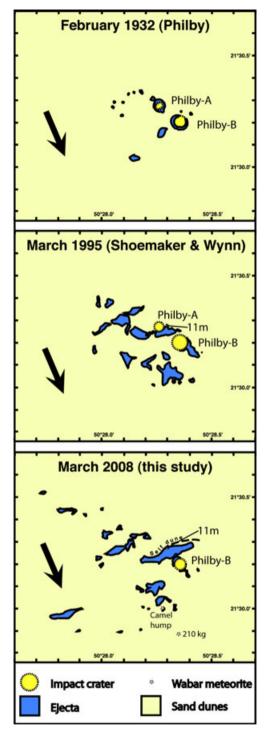

Fig. 3. Maps based on Philby (1933a), Shoemaker and Wynn (1997), Wynn (2002), and this study, showing a strong variation in size and shape of ejecta blanket due to moving sand dunes. On all maps, the ejecta field to the west of the craters is larger than on the east. Note that the 11 m crater was covered when Philby visited the place (1932), that Philby-A is now under a seif dune, and that the 11 m crater is partially covered in March 2008. The map produced in this study also shows the location of the largest iron meteorites that fell as individuals. Arrow indicates main direction of dune movement.

Only crater Philby-B and large parts of the 11 m crater (Figs. 2 and 3) were exposed at the time of our visit in March 2008. Crater Philby-A was fully covered by a dune.

Extension and Nature of Ejecta Material

The craters and impact ejecta fields (Fig. 3) were mapped by two of us (EG, BAH) using handheld GPS. The resulting map demonstrates important changes since the mapping by Shoemaker and Wynn in 1995 (Fig. 3). We could significantly extend the area covered by ejecta to the NW and SW. We also redraw the map of Philby (1933a) for comparison, using the two large craters for reference (Fig. 3).

Assuming that the sand dune mapped by Philby (1933a) to the north of his A crater is the same as the one that completely covered Philby-A in 2008 (Wynn 2002), we calculate an average advancement of the dunes in a southerly direction of 1.6 m yr^{-1} over the last 76 yr. Based on images taken by Shoemaker and Wynn in 1995, an advancement of 13 m between 1995 and 2008 is estimated (1.0 m yr^{-1}), and an aerial image taken by George Steinmetz in 2002, compared with a 2010 satellite image, yields an advancement rate of 1.1 m yr^{-1}. QuickBird high-resolution satellite images acquired on February 9, 2009 (Fig. 4) and in 2012 (Bing maps) indicate an advancement of 2.0 m yr^{-1} during this period. The 2009 image shows that the 11 m crater is about 60% covered by sand, while it was completely covered in 2012. In the period 2008–2012, only parts of the rim of Philby-B were exposed, whereas Philby-A was entirely covered by a sand dune. By extrapolation, using these observations, we can expect the northern rim of Philby-A to reappear no earlier than 2050. For the next few decades, only Philby-B will be visible.

During our field investigation, we recovered fragments of completely oxidized iron meteorites, from the ejecta blanket close to both the 11 m crater and Philby-B crater. These fragments range up to 5 cm in size (Fig. 5). Wynn and Shoemaker (1998) found similar objects up to 10 cm in size. This "iron shale" shows intense fracturing due to the volume increase during oxidation and a flaky texture characteristic of many such occurrences of meteorite oxide (Buddhue 1957). Polished sections only show microscopic traces of unoxidized metal enclosed in oxides/hydroxides. Minerals observed in the oxidation assemblages include iron hydroxides, magnetite, and maghemite. A green oxidation phase has been identified as reevesite, $Ni_6Fe^{3+}_2(CO_3)(OH)_{16}\cdot 4H_2O$, by combined XRD and EDS. One oxidized iron fragment is covered by impact glass, and we observed numerous impact melt specimens
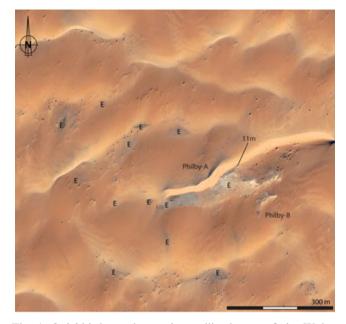

Fig. 4. Quickbird panchromatic satellite image of the Wabar impact site, acquired on February 10, 2009. 11 m = 11 m crater; E = ejecta blanket, white areas dominated by white lithified sand, dark areas dominated by black impact glass. Black dots are shrubs, mainly *Cornulaca Arabica*.

with small fragments of adhering oxidized meteoritic iron. Similar observations were made by Wynn (2002).

Shock-Lithified and Shock-Melted Sand

The Wabar impact caused shock lithification and shock bleaching of the unconsolidated sand material, resulting in a significantly brighter appearance of the white shock-lithified dune sand ("insta-rock" of Wynn and Shoemaker 1998) as compared with the brownish-yellow unshocked sand. In the most consolidated shock-lithified sands, the grains are fused due to both localized and penetrative shock-melting. In all larger fragments of shock-lithified sand found in and near the craters, we consistently observed that the sedimentary bedding is perfectly preserved (Fig. 5a). Lithified fragments commonly show open fractures (Figs. 5b and 5c) predominantly oriented roughly perpendicular to the bedding, and slickenside features across or along bedding planes. Bedding planes may also be bent, and beds detached from each other. Radiating striations are less common and show some similarities with shatter cones (Fig. 5c). Moreover, open fractures are oriented perpendicular to the striation (Fig. 5c).

We observed several well-preserved fossilized animal burrows, approximately 8 mm in diameter and originally sand-filled, in the shock-lithified dune sand (Fig. 5b). This demonstrates that instant shock-fossilization is possible at an impact site. According to a survey among invertebrate specialists, the observed
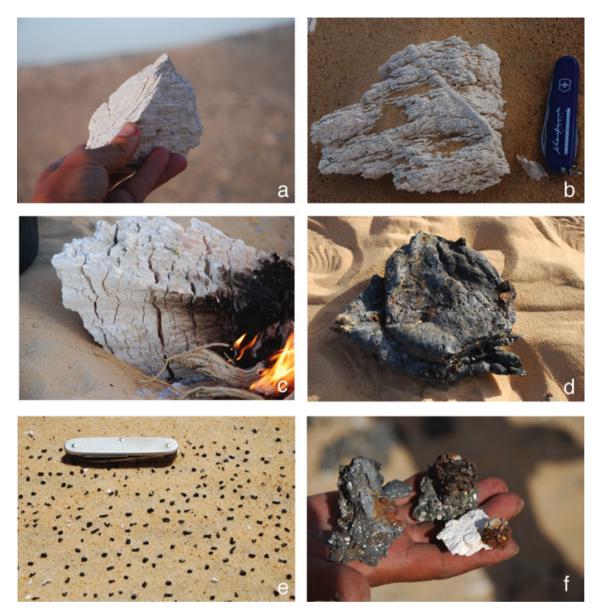
Fig. 5. Shock-lithified sand and ejecta. a) Shock-lithified sand displaying horizontal primary bedding as well as shock-induced foliation and tension gashes perpendicular to the bedding. b) Perfectly preserved animal (most likely spider) burrow in shock-lithified dune sand. c) Rare occurrence of fan-shaped striation resembling shatter cone structures in shock-lithified sand. The block is approximately 40 cm in size. d) 30 cm large black ejecta "bomb" of vesicular glass from the proximal part of the ejecta field containing fragments of white shock-lithified sand. e) Millimeter-sized melt droplets dominate the distal parts of the ejecta field. Knife length is 9 cm. f) Strongly shattered and completely altered iron meteorite fragments within melted rocks (frequent), and in association with white shock-lithified sand (rare; probably agglutinated during weathering).

animal burrows were most likely produced by burrowing spiders.

In the ejecta material, there is a gradual transition from shock-lithified sand to completely fused white-greenish, vesicular quartz glass (lechatelierite) and then, with admixture of meteoritic components, to black, vesicular glass (e.g., Spencer and Hey 1933; Wynn 2002). Characteristically, the larger black glass fragments (Fig. 5d) contain fragments of white, shock-lithified sand in their interior. Larger glass fragments are strongly vesicular. Tests carried out in the laboratory show that, due to the high content of impact-induced vesicles, many glass fragments float in water. Black glass droplets are vesicle-poor and show less schlieren than the white-greenish and black glass bombs.

We have counted the number of fragments of meteorite oxide, shock-lithified sand, white-greenish

glass, black glass bombs (generally >5 cm and vesicular), and black glass droplets (generally <5 cm and vesicle-free) at several localities in the ejecta field (Fig. 6). The resulting map demonstrates that meteorite fragments and white-greenish glass only occur in the vicinity of the impact craters. Large fragments of shock-lithified sand are concentrated around the craters, whereas smaller white fragments of shock-lithified sand can also be found at larger distances from the craters. These are mainly from disintegrated black glass bombs, where they occur as angular inclusions or form a core piece wrapped entirely by black melt. The amount of black glass droplets increases to the NW (Fig. 6). This is probably due to an interference of the ejecta blankets produced by Philby-A and Philby-B. Hence, it does not yield information about the entry direction of the impactor.

While the shock-lithified sand derived from craters Philby-A and -B is quite hard, the sand below the 11 m crater is only weakly lithified. At this site, stratification is also preserved, but the rock remains very soft and friable while showing the same white appearance (shock bleaching) as more strongly shock-lithified sand.

Slickenside surfaces (striations are parallel) indicate postshock movements in the already lithified material during or immediately after impact.

Thin sections prepared from shock-lithified sand, ranging from weakly compacted varieties (from below the 11 m crater) to white, massive shock-lithified sand, show characteristic shock features in quartz grains (Fig. 7). In weakly shocked sand from below the 11 m crater (WB08-2; Figs. 7a and 7b), quartz grains are strongly fractured, mainly at grain contacts. It appears that lithification and bleaching apparently are only due to compaction of crushed quartz grains and reduction of pore space. Many larger grains display a characteristic set of subparallel or radiating concussion fissures (Kiefer 1971; Fig. 7b). Some sand grains survived without obvious shock effects. In the next shock level (WB08-4; Figs. 7c and 7d), all quartz grains are shocked, as seen by strong mosaicism, formation of PFs, and the presence of several sets of PDFs. Sample WB08-7 (Figs. 7e and 7f) shows, in addition, partial fusion of the matrix (presence of abundant quartz glass, or lechatelierite). Like Chao et al. (1961), we did not observe diaplectic quartz. X-ray diffractometry of powdered, untreated samples, and of samples treated with dilute hydrofluoric acid to remove quartz (Appendix S2), showed the presence of significant amounts of coesite in WB08-4 (approximately 3 wt%) and WB08-7 (approximately 7 wt%), but no coesite was detected in the weakly shocked sample from the 11 m crater (WB08-2). Approximately 2 wt% stishovite was identified in sample WB08-4 (Fig. S1).
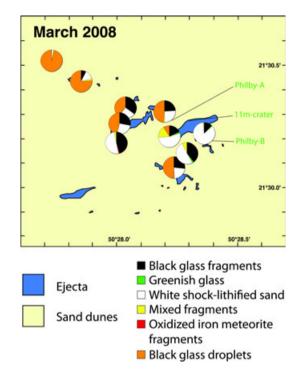

Fig. 6. Map showing the distribution of different ejecta material, as mapped in March 2008. Pie plots show the relative abundance of different ejecta materials. Note that oxidized iron meteorite fragments and green glass are only found in vicinity of the craters, whereas the abundance (but not the size) of melt droplets increases to NW, but the relative abundance of fragments of white shock-lithified sand decreases.

WB08-1, 3, 4 (Figs. 7c and 7d) are ejected shock-lithified dune sands collected between Philby-B and 11 m crater. WB08-2 (Figs. 8a and 8b) is a weakly consolidated shocked sand from below the 11 m crater. It shows irregular fracturing of some quartz grains, but neither PFs nor PDFs have been observed. In WB08-1, quartz grains have irregular extinction. Some grains display irregular and subparallel fractures, and concussion figures (Kiefer 1971). Generally, there is intense fracturing of quartz, but no PDFs were observed in thin sections and no coesite was detected by XRD. WB08-3 shows irregular extinction of quartz and irregular, subparallel fractures. Quartz shows intense fracturing and generally more than one set of poorly penetrative and undecorated PDFs per grain. Crystallographic indexing of eight grains indicates that the most common PDF orientations have Miller indices of $\{10\bar{1}3\}$ and $\{10\bar{1}2\}$ (Table 2). WB08-03 shows presence of approximately 12 wt% coesite (XRD). Sample WB08-4 shows irregular extinction of quartz; irregular, subparallel fractures; and occasional PFs. The quartz fracturing is intense and undecorated PDFs are present. Fewer grains contain PDFs in comparison with
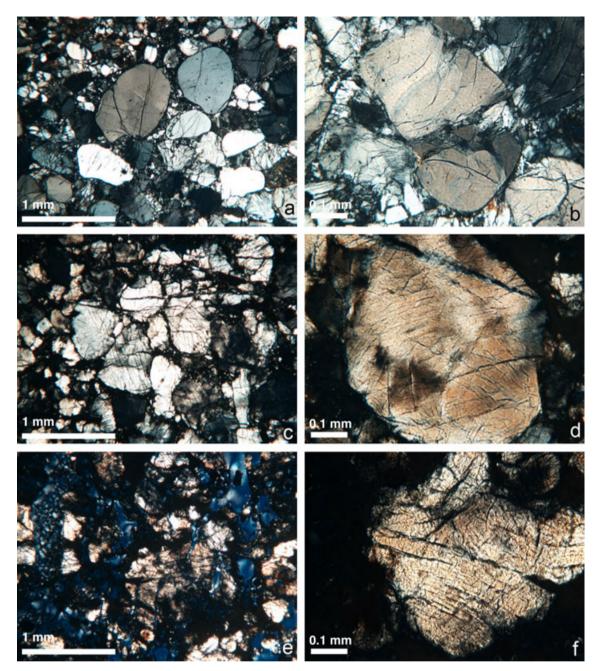
Fig. 7. Photomicrographs of shock-lithified Wabar sand (transmitted light, crossed polarizers). a) WB08-2, friable shock-lithified sand from the 11 m crater. Partial crushing of rounded quartz grains, all fractures are irregular. b) Crushed sand grain in WB08-2, friable shock-lithified sand, 11 m crater. c) WB08-4, shock-lithified sand, ejecta from large craters. Quartz grains show strong mosaicism and development of planar fractures. d) WB08-4, shock-lithified sand, ejecta from large craters. Single quartz grain showing several sets of planar deformation features. e) WB08-7, strongly shocked and partially molten shock-lithified sand, ejecta from large craters. Quartz grains show strong mosaicism and development of planar fractures. Glass is black, pore space, dark blue. f) WB08-7, strongly shocked and partially molten shock-lithified sand ejecta from large craters. Strongly shocked single quartz grain showing several sets of planar deformation features.

WB08-3. XRD analysis shows that this sample contains approximately 7 wt% coesite. Measurements and indexing of eight grains (Table 2) indicate that the most common orientation of the PDFs is $\{10\bar{1}3\}$.

According to Brett (1967) and Gibbons et al. (1976), Fe-Ni spherules are abundant in the black and white-greenish melts, but almost totally absent in the black melt tears. Mittlefehldt et al. (1992) showed that

Fig. 8. X-ray fluorescence data plot of Fe versus Ni in individual small impact glass fragments, and of different areas in two large cuts of vesicular impact glass fragments. The line is a mixing line between Wabar iron (Mittlefehldt et al. 1992) and local dune sand (Tables 3 and 4). One of the large glass samples (40020.2) is depleted in Ni relative to Fe, while the other (40020.1) shows Fe/Ni similar to that of the Wabar iron meteorite. The small glass fragments show generally higher admixtures of meteoritic material and larger variations of Fe/Ni than larger fragments.

the concentration of siderophile elements in the glasses increases from vesicle-rich bombs to vesicle-free glass droplets, indicating an increasing meteoritic component. This has been explained by a propagating shock front, where the highest temperatures are reached in the highest stratigraphic position. In parallel, the impactor also reaches high temperatures, facilitating the mixing with heated target material.

Cathodoluminescence investigations reveal color zoning in quartz, indicating partial re-equilibration. In weakly shock-lithified sand (Fig. S2a), many shattered quartz grains show a reddish luminescence color, indicating sand grains of volcanic origin (Götze et al. 2001; Augustsson and Reker 2012). Grains with darker luminescence colors are of plutonic or metamorphic origin. Partially molten shock-lithified sand displays dark blue quartz grains with light-colored rims (transformation to glass; Fig. S2b). Upon complete melting, quartz is transformed into a relatively homogeneous quartz glass showing a bright light blue luminescence (Fig. S2c). The increased amount of Fe-Ni in the black glass suppresses the luminescence signal. However, a white shock-lithified sand shows quartz

Table 2. Miller indices of indexed PDF sets in quartz grains of shock-lithified sand.

Grain	Number of sets and orientations
Sample WB08-3	
1	1; {$10\bar{1}3$}
2	3; {$10\bar{1}3$}, {$10\bar{1}3$}, {$10\bar{1}2$}
3	4; {$10\bar{1}3$}, {$10\bar{1}3$}, {$10\bar{1}4$}, unindexed
4	5; {$11\bar{2}2$}, {$10\bar{1}2$}, {$10\bar{1}3$}, 2x unindexed
5	3; {$10\bar{1}1$}, {$10\bar{1}3$}, unindexed
6	2; {$10\bar{1}3$}, {$10\bar{1}2$}
7	2; {$11\bar{2}2$}, {$10\bar{1}2$}
8	2; {$10\bar{1}3$}, unindexed
Sample WB 08−4	
1	3; {$10\bar{1}3$}, {$10\bar{1}3$}, unindexed
2	1; {$10\bar{1}3$}
3	1; {$11\bar{2}2$}
4	3; {$10\bar{1}4$}, {$10\bar{1}3$}, {$10\bar{1}4$}
5	2; {$10\bar{1}3$}, {$10\bar{1}3$}
6	2; {$10\bar{1}3$}, {$10\bar{1}2$}
7	1; {$10\bar{1}3$}
8	2; {$10\bar{1}3$}, {$10\bar{1}3$}

grains with luminescence color zonation, due to heating by the impact glass and, possibly, decompression (Fig. S2d).

Composition of Target Materials, Impact Melts, and Meteorite Oxide

Previous analyses of ejecta samples (Spencer and Hey 1933) showed 87.45 wt% SiO_2, 5.77 wt% FeO, 0.28 wt% Fe_2O_3, and 0.35 wt% NiO. The white-greenish shock-molten sand has a SiO_2 content of 92.88 wt%. More detailed analyses on the black melt droplets ("pearls") and ejecta ("bombs") and white-greenish glass collected in the early 1960s (Holm 1962) were given by Ehmann (1962), Brett (1967), Morgan et al. (1975), Gibbons et al. (1976), Hörz et al. (1989, 1991), and Mittlefehldt et al. (1992). Hörz et al. (1989) showed that projectile dissemination in large, black vesicular glass bombs is heterogeneous. This observation was confirmed by Mittlefehldt et al. (1992), who reported that the small beads have higher percentage of meteoritic material included in the melt (10–17%) than the massive, vesicular melts (<5%). The smallest beads also contain fever vesicles, and fewer Fe-Ni spheres.

Impact glasses (IG), shock-lithified sand (SLS), and dune surface sand (SS) from the area were analyzed by XRF (Table 3) and by ICP-OES/ICP-MS and INAA (Table 4; Appendix S2). Due to numerous small inclusions of quartz and other oxides, the fulgurite glass (Table 4) was analyzed by electron microprobe. It provides a reference of fused local sand without
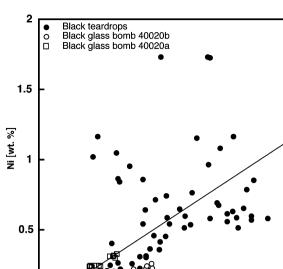
Table 3. X-ray fluorescence analyses of dune sand and different ejecta from the Wabar craters.

	Sand	σ	SLS	σ	11 m SLS	σ	Pearls	σ	40020.1	σ	40020.2	σ
n	17		16		6		71		23		31	
Al_2O_3	1.64	1.30	0.96	0.62	1.44	0.19	2.25	1.19	0.85	0.19	1.02	0.38
FeO	0.85	0.45	0.48	0.05	0.53	0.05	8.65	4.44	3.41	1.49	5.62	1.89
CaO	4.27	4.48	0.70	0.25	0.76	0.28	1.89	0.92	1.06	0.15	1.15	0.29
K_2O	0.73	0.35	1.06	0.34	1.12	0.12	1.00	0.23	0.94	0.10	1.08	0.18
Ti	1337	1218	449	117	584	115	1076	381	716	112	716	102
Ni			<14				5881	3863	1944	966	1712	564
Rb	17	6	22	5	23	2	21	5	23	2	26	2
Sr	85	39	60	13	70	11	74	15	73	5	79	7
Zr	230	150	53	26	72	33	120	26	89	17	101	31
Fe/Ni							14.8	5.9	13.8	1.4	26.1	2.4

SLS = Shock-lithified sand; Pearls = black glass droplets; 40020.1 and 40020.2 are black impact glasses. Major elements in wt%, trace elements in ppm.

meteoritic component. A slightly increased Fe content as seen in the shock-melted glass is not seen in the fulgurite sample (Table 4).

The IG samples include 71 different black teardrop glasses (Glasses in Table 3) and repeat analyses (23 and 31) of different spots from large individual black glasses of bombs (Fig. 8). Glass analyses on mixing line (squares) are from a cut section of a vesicular black glass bomb containing partially fused shock-lithified sand inclusion (40020.1; see also Table 3). Average compositions of SLS and SS are very similar, with somewhat lower concentrations of Fe, Zr, Ti in SLS, indicating variable contents of heavy minerals. Importantly, there are no increased concentrations of Ca and Sr in IG and SLS, demonstrating the absence of a component derived from the limestone bedrock below the sand sheet. The sand sample 40024 (Table 4), collected 6.3 km NW of Wabar, shows a higher CaO content due to the presence of limestone outcrops in the vicinity. The relationship between Fe and Ni contents shows a number of interesting features. One of the large, vesicular glasses (40020.1 in Table 3) indicates that the mixing between Wabar iron and dune sand shows no fractionation of Fe from Ni (Fig. 8), while the other large glass sample (40020.2 in Table 3) shows Ni-depletion. The latter is comparable to experimental work by Ebert et al. (2013) and earlier studies on Wabar material (Mittlefehldt et al. 1992). The small glass samples show a wide variation with Fe/Ni higher and lower than Wabar iron (Fig. 8). This may be explained by a certain degree of decoupling of Ni-enriched, partially oxidized metal melt droplets and silicate melt preferentially enriched in FeO during the mixing process. Small glass fragments that are Ni-enriched contain microscopic metal droplets at the surface. The mean Fe/Ni of one large IG 40020.1 is 13.8, close to the value for Wabar iron (12.4). The

samples analyzed by XRF (Table 3) show a wide range of meteorite admixture from 0 to approximately 16%, with many samples containing about 10% of meteoritic material (based on Fe and Ni).

New major and trace element analyses of meteorite oxide, unshocked and shock-lithified sand, black vesicular glass, and a fulgurite are presented in Table 4 and compared with literature data. Our sample of unshocked sand (sand in Table 3), collected some 6 km NW of Wabar, has higher concentrations of elements typically present in heavy minerals, as well as of Ca and Sr, than the shock-lithified sand, which is rather poor in Zr, Ti, Ca, and Sr. This demonstrates that the sand sheet is not homogeneous and locally contains wind-blown bedrock material, but not at Wabar. The black vesicular glass sample 40020.1 (Tables 3 and 4) has similar concentrations of Zr, Ti, Ca, and Sr as the shock-lithified sand and drift sand data reported by Hörz et al. (1989). These data demonstrate the absence of limestone bedrock in the impact melts. The meteoritic component in the glass sample 40020.1 is 5.4–6% based on Ni and Fe, and approximately 4% based on platinum group elements.

We analyzed the oxygen isotopic composition of black impact glass droplets (Table 5) to test whether there was any evidence for nonmass-dependent fractionation of O isotopes within the impact vapor cloud. The data (Table 5) plot on the terrestrial fractionation line ($\Delta^{17}O = +0.01‰$). These results are consistent with mixing of partly oxidized iron meteorite material and terrestrially derived sand to form the impact glass, with fractionation during oxidation of the meteorite component following the terrestrial fractionation line. The $\delta^{18}O$ values of 12.4 ‰ are in the range typical for sand seas (Yang et al. 2008) and correspond to those of quartz derived from magmatic or metamorphic source rocks.

Table 4. Elemental composition of materials from the Wabar site

Number Sample	Wabar iron[a]	40016 Ox Met	40020.1 Black glass	40024 SS	40005 SLS	40010 SLS	SS[b]	White glass[b]	Fulgurite[c]
SiO_2			86.08	84.24	93.93	94.04	93.6	93.0	99.68
TiO_2			0.105	0.345	0.083	0.075	0.12	0.11	0.06
Al_2O_3			2.51	3.12	2.34	2.19	2.56	2.45	bd
Fe_2O_3 (tot)		80.92	8.33	1.44	0.36	0.36	0.36	0.67	0.01
Fe	91.6								
Ni	7.38								
MnO			0.017	0.03	0.008	0.009	0.01	0.01	bd
MgO			0.49	0.81	0.27	0.31	0.47	0.47	bd
CaO			1.25	4.44	0.64	0.86	1.16	1.01	bd
Na_2O			0.62	0.58	0.38	0.36	0.52	0.46	bd
K_2O			0.97	0.9	1.05	0.91	1.06	1.02	0.01
P_2O_5		0.18	0.04	0.05	0.02	0.03	0.02	0.01	
LOI		5.60	−1.49	3.73	0.99	1.12			
Total			98.92	99.68	100.10	100.30	99.88	99.21	99.76
Sc			1	3	1	<1	0.83	1.23	
V			16	35	15	14			
Cr	88		90	360	20	30	78	73	
Co	5000		290	3	19	9	2	28	
Ni		44000	4040	20	<20	<20	44	430	
Cu	167		<10	<10	<10	<10			
Zn			<30	<30	<30	<30			
Ga	18.4		3	3	2	2			
Ge	38.3		1.9	1	0.8	0.8			
As			<5	<5	<5	<5			
Rb			21	19	22	19	18	24	
Sr			81	126	76	71			
Y			4.2	8.5	3	2.8			
Zr			87	489	80	64	40	80	
Nb			1.8	4	1.4	1.1			
Sb			<0.2	0.4	0.2	<0.2		0.12	
Cs			0.4	0.5	0.4	0.4	0.33	0.44	
Ba			256	245	270	217	230	240	
La			6.6	8.2	3.9	3.6	3.8	4.5	
Ce			10.7	16.0	7.4	6.8	7.5	8.4	
Pr			1.3	2.0	0.9	0.8			
Nd			5.0	7.7	3.5	3.3	3.6	4.1	
Sm			0.99	1.6	0.64	0.67	0.7	0.79	
Eu			0.25	0.35	0.16	0.18	0.17	0.21	
Gd			0.78	1.28	0.53	0.52			
Tb			0.12	0.23	0.09	0.08	0.11	0.09	
Dy			0.72	1.42	0.54	0.50			
Ho			0.15	0.31	0.11	0.10			
Er			0.45	0.95	0.33	0.30			
Tm			0.07	0.14	0.05	0.05			
Yb			0.47	1.05	0.37	0.31	0.32	0.43	
Lu			0.08	0.19	0.07	0.05	0.05	0.07	
Hf			2.2	10.8	1.8	1.4	1.2	2.59	
Ta			0.17	0.40	0.54	0.32	0.1	0.11	
Pb			30	6	<5	<5			
Bi			<0.1	<0.1	<0.1	<0.1			
Th			1.49	3.68	1.06	0.96	0.86	1.17	
U			0.54	1.14	0.4	0.41	0.45	0.45	
Ru (ppb)		3.28	0.21						
Rh (ppb)		0.45	0.38						

Table 4. *Continued.* Elemental composition of materials from the Wabar site.

Number Sample	Wabar iron[a]	40016 Ox Met	40020.1 Black glass	40024 SS	40005 SLS	40010 SLS	SS[b]	White glass[b]	Fulgurite[c]
Pd (ppb)		0.96	0.066						
Re (ppb)	0.85	0.15	0.017						
Os (ppb)		1.5	0.14						
Ir (ppb)	8.1	2.58	0.30				<2	36	
Pt (ppb)	13.1	5.99	0.51						
Au (ppb)	0.56	0.24	0.021				<5	12	

Ox Met = oxidized iron meteorite fragment ("iron shale"); SLS = shock-lithified sand; SS = surface sand; bd = below detection. Major elements in wt%, trace elements in ppm (except as noted).
[a]Mittlefehldt et al. (1992).
[b]Hörz et al. (1989).
[c]Electron microprobe.

Table 5. Oxygen isotopes of black impact glass.

Sample	Comments	$\delta^{17}O\%$	$\delta^{18}O\%$	$\Delta^{17}O\%$
Wabar 08-61	Black melt glass	6.48	12.44	0.01
Wabar 08-62	Black melt glass	6.46	12.41	0.01

DISCUSSION

Our observations prove that the Wabar craters are located within a geologically active dune field and cannot be considered as stable over hundreds of years.

The Number of Craters and the Distribution of Iron Meteorite Fragments and Ejecta

Although Philby (1933a, 1933b) mentioned possibly four different craters, he only mapped two (see Fig. 3). The other two craters were only inferred on the basis of isolated ejecta patches around sand dunes. From the data now available (Fig. 3), we conclude that there are most likely only three impact craters. Moreover, as Abercrombie (1966) mentions three closely spaced craters, we assume that the 11 m crater described by Wynn and Shoemaker (1998) is included in this count.

Exposure of the ejecta field is patchy and highly variable due to the moving sand, and the two possible crater locations suggested by Philby (1933a) are only part of the ejecta field.

The 11 m crater yields important hints about the timing of crater formation. Whereas the ejecta curtains from the larger two craters seem to have interfered and material was deflected to the NW, the 11 m crater formed before the fallout of ballistically dispersed black glass, not present on the compacted 11 m crater floor.

The presence of strongly shattered iron meteorite fragments ("shrapnels") together with meteorites displaying regmaglyptic surfaces, unaffected by the forces of high-velocity impact, has recently been reported from the Kamil crater in Egypt (D'Orazio et al. 2011). These authors also concluded that subparallel, undulating fractures in iron fragments are related to the terrestrial impact, whereas irons displaying regmaglyptic surfaces arrived as individual, more strongly decelerated objects.

Entry Direction and Age of the Impact

The estimation of an entry from WNW by Passey and Melosh (1980) was based on Philby's (1933a) map showing two questionable craters C and D that are now clearly obsolete. Wynn and Shoemaker (1998) and Wynn (2002) estimated that the impactor arrived from about 300° (NW) at an angle of less than 22° from the horizontal to explain the observed asymmetry of the ejecta field (especially the white shock-lithified sands). They also estimated a final impact velocity of about 5–7 km s^{-1}, and object sizes of 8.0 to 9.5 m diameter to produce the largest crater. The distance from center to center between the two large craters is approximately 200 m. However, the nicely ablated 2040 kg fragment ("camel hump"; Figs. 2a and 3) was found at a distance of approximately 420 m SSW of the center of the largest crater Philby-B (Fig. 3). Moreover, the 210 kg iron (Figs. 2b and 3) was found at a distance of approximately 600 m to the south of the Philby-B center. Thus, from the field relationships, it likely that these two more strongly decelerated iron meteorite fragments reached the ground with some delay and fell at the rim and outside the crater ejecta blanket (Fig. 3). In comparison with other strewn fields (e.g., Llorca et al. 2005; Gnos et al. 2009), the distribution of craters and individually fallen iron fragments displaying regmaglyptic surfaces seems consistent with arrival of the bolide from the south.

It can be estimated that the iron meteorite fragment forming the 11 m crater was similar in size (Table 1) to the 2040 kg iron (Table 1). Apparently, the latter piece

separated at high altitude, achieved a stable flight position, and was decelerated, whereas the fragment causing the 11 m crater had a higher velocity due to later detachment from a larger mass and arrived approximately contemporaneous with the largest two fragments. The accumulation of fragments of shock-lithified sand between the two craters Philby-A and Philby-B may be due to interferences of the two ejecta blankets, or due to the presence of a sand dune in this area.

We can assume that the largest piece that created the 116 m crater (Philby-B) hit the sand first, followed shortly thereafter by the second fragment. The pressure wave created by the first impact must have affected the ejecta of the second, deflecting them to the NW (Fig. 3). Although winds may have had an influence on the smallest particles, this is hardly the reason for the observed asymmetry of the ejecta field. Rather, the ejecta blanket from Philby-B crater has deviated from the one developing at Philby-A crater, and is most likely to be the main reason why the ejecta field is so strongly asymmetric (Melosh 2007). Thereafter, the 11 m crater formed, before fallout material enriched in impactor material covered it.

Our data are consistent with the interpretation of Basurah (2003), who correlated the Wabar impact event with the description, given in two historic poems, of a bright fireball on September 1, 1704, observed in Tarim, Yemen (Fig. 1), 620 km SSW of Wabar. This is consistent with a trajectory of the bolide from south to north, as indicated by the distribution of meteorites and craters.

Impact Shock Pressure

The friable shock-lithified sand below the 11 m crater (Fig. 2d) displays cracked quartz (Figs. 7a and 7b) lacking PDFs and coesite due to lower shock pressures. However, concussion figures are common. Although it is beyond doubt that this rock was affected by impact, they indicate that clear PDFs only develop when the existing pore space has been destroyed by compaction. According to Grieve et al. (1996), this would correspond to shock class Ia (without coesite or glass) and a shock pressure of approximately 3 GPa.

Planar microstructures in quartz are found in authochthonous and ejected shock-lithified sand samples derived from the two larger craters. They also commonly contain coesite and stishovite. Formation of lechatelierite starts above approximately 30 GPa at temperatures of >1000 °C in porous material (shock class IV of Grieve et al. 1996). The absence of diaplectic quartz in studied shock-lithified sand from Wabar indicates a direct transition from strongly shocked quartz grains to lechatelierite.

Dynamics of Lithification and Impact Melt Formation

Considering the unconsolidated nature of the target, it is evident that the formation of slickensides, radial striations (resembling shatter cones; Fig. 5c), and of extensional cracks (Fig. 5c) must all postdate shock lithification.

Shock temperatures in porous material are an order of magnitude higher than in compact crystalline material (e.g., Stöffler and Langenhorst 1994). This may explain why first droplets with higher contribution of meteoritic material (enhanced in Fe-Ni) form.

The impact melts contain both FeO and spherules of unoxidized metal enriched in Ni (Hörz et al. 1991; Mittlefehldt et al. 1992). Significant amounts of meteoritic iron must have been oxidized to FeO in the impact vapor plume, adding energy to the event. The impact melt samples show a fractionation of Ni and Fe (Fig. 8), most likely due to a partial separation of portions of the impact cloud enriched in $FeO-SiO_2$, and metal spherules, respectively. A higher contribution from the iron meteorite to the melt not only lowers the melting point but also the viscosity of the melt. This viscosity reduction can be clearly demonstrated by comparing irregular-shaped white-greenish glass ejecta showing rough surface with aerodynamically shaped, smooth black glass droplets. Whereas large black glass bombs are strongly vesicular and contain abundant clasts of shock-lithified sand, melt droplets completely degassed and show higher amounts of dissolved projectile material (e.g., Hörz et al. 1991). For this reason, they are less viscous and can easily degas, whereas vesicles form in the more viscous material. Comparable to the white-greenish impactor-poor impact glass, the fulgurite glass formed by lightning also displays abundant vesicles. A particularly important observation is the transformation of loose dune sand into a solid rock with perfect maintenance of sedimentary texture and even animal burrows during the process of shock lithification.

Site Protection

Our observations prove that the Wabar craters are located in a geologically active dune field, which is evolving rapidly and shows dramatic changes in periods of as little as a few hundred years.

Our visit to the Wabar crater field in the dynamic sand sea of the Rub' al Khali demonstrated the vulnerability of this unique young impact crater site. We observed degradation of the impact features by wind (erosion and covering by sand) as well as by human interference. The most damaging interference appears to be the driving of cars and trucks on the

ejecta surfaces. It would be highly desirable to take measures that this is avoided.

Editorial Handling—Dr. Alexander Deutsch

REFERENCES

Abercrombie T. J. 1966. Saudi Arabia. Beyond the sands of Mecca. *National Geographic* 1291:1–53.

Augustsson C. and Reker A. 2012. Cathodoluminescence spectra of quartz as provenance indicators revisited. *Journal of Sedimentary Geology* 82:559–570.

Basurah H. M. 2003. Estimating a new date for the Wabar meteorite impact. *Meteoritics & Planetary Science* 38:A155–A156.

Bramkamp R. A. and Ramirez L. F. 1959. *Geologic map of the northwestern Rub' al Khali quadrangle, Kingdom of Saudi Arabia, map I-213 A*. Washington, D.C.: U.S. Geological Survey.

Brett R. 1967. Metallic spherules in impactite and tektite glasses. *American Mineralogist* 52:721–733.

Buchwald V. F. 1975. *Handbook of iron meteorites*. Berkeley: University of California Press. 1418 p.

Buddhue J. D. 1957. *The oxidation and weathering of meteorites*. Albuquerque: University of New Mexico Press. 161 p.

Chao E. C. T., Fahey J. J., and Littler J. 1961. Coesite from the Wabar crater, near Al Hadida, Arabia. *Science* 133:882–883.

D'Orazio M., Folco L., Zeoli A., and Cordier C. 2011. Gebel Kamil: The iron meteorite that formed the Kamil crater (Egypt). *Meteoritics & Planetary Science* 46:1179–1196.

Ebert M., Hecht L., Deutsch A., and Kenkmann T. 2013. Chemical modification of projectile residues and target material in a MEMIN cratering experiment. *Meteoritics & Planetary Science* 48:134–149.

Edgell H. S. 2006. *Arabian deserts. Nature, origin and evolution*. Dordrecht: Springer.

Ehmann W. D. 1962. The abundance of nickel in some natural glasses. *Geochimica et Cosmochimica Acta* 26:489–493.

Gibbons R. V., Hörz F., Thompson T. D., and Brownlee D. E. 1976. Metal spherules in Wabar, Monturaqui, and Henbury impactites. Proceedings, 7th Lunar Science Conference. pp. 863–880.

Gnos E., Lorenzetti S., Eugster O., Jull A. J. T., Hofmann B. A., Al-Kathiri A., and Eggimann M. 2009. The Jiddat al Harasis 073 strewn field, Sultanate of Oman. *Meteoritics & Planetary Science* 44:375–387.

Götze J., Plötze M., and Habermann D. 2001. Origin, spectral characteristics and practical applications of the cathodoluminescence (CL) of quartz—A review. *Mineralogy and Petrology* 71:225–250.

Grady M. M. 2000. *Catalogue of meteorites*, 5th ed. Cambridge, UK: Cambridge University Press. 689 p.

Grieve R. A. F. 1987. Terrestrial impact structures. *Annual Review of Earth and Planetary Sciences* 15:245–270.

Grieve R. A. F., Langenhorst F., and Stöffler D. 1996. Shock metamorphism of quartz in nature and experiment: II Significance in geoscience. *Meteoritics & Planetary Science* 31:6–35.

Holm D. A. 1962. New meteorite localities in the Rub' al Khali, Saudi Arabia. *American Journal of Science* 260:303–309.

Holsapple K. A. 1993. The scaling law of impact processes in planetary sciences. *Annual Review of Earth and Planetary Sciences* 21:333–373.

Hörz F., See T. H., Murali A.V., and Blancherd D. P. 1989. Heterogeneous dissemination of projectile material in impact melts from the Wabar crater, Saudi Arabia (abstract). 19th Lunar and Planetary Science Conference. p. 697.

Hörz F., Mittlefehldt D. W., and See T. H. 1991. Dissemination and fractionation of projectile material in impact melts from the Wabar crater, Saudi Arabia. *Meteoritics* 26:346–347.

Kiefer S. W. 1971. Shock metamorphism of the Coconino sandstone of Meteor Crater, Arizona. *Journal of Geophysical Research* 76:5449–5479.

Llorca J., Trigo-Rodriguez J. M., Otiz J. L., Docobo J. A., Garcia-Guinea J., Castro-Tirado A., Rubin A. E., Eugster O., Edwards W. N., Laubenstein M., and Casanova I. 2005. The Villabeto de la Peña meteorite fall: I: Fireball energy, meteorite recovery, strewn field and petrography. *Meteoritics & Planetary Science* 40:795–804.

Melosh H. J. 2007. A hydrocode equation of state for SiO_2. *Meteoritics & Planetary Science* 42:2079–2098.

Mittlefehldt D. W., See T. H., and Hörz F. 1992. Dissemination and fractionation of projectile materials in the impact melts from Wabar Crater, Saudi Arabia. *Meteoritics* 27:361–370.

Morgan J. W., Higuchi H., Ganapathy R., and Anders E. 1975. Meteoritic materials in four terrestrial meteorite craters. Proceedings, 6th Lunar Science Conference. pp. 1609–1623.

Passey Q. R. and Melosh H. J. 1980. Effects of atmospheric breakup on crater field formation. *Icarus* 42:211–233.

Philby H. S. J. 1933a. *The empty quarter*. London: Constable and Company Ltd. 433 p.

Philby H. S. J. 1933b. Rub' al Khali: An account of exploration in the Great South Desert of Arabia under the auspices and patronage of his majesty 'Abdul 'aziz ibn Sa'ud, King of Hejaz and Nejd and its dependencies. *Geographical Journal* 81:1–21.

Prescott J. R., Robertson G. B., Shoemaker C., Shoemaker E. M., and Wynn J. 2004. Luminescence dating of the Wabar

meteorite craters, Saudi Arabia. *Journal of Geophysical Research* 109:1–8.

Shoemaker E. M. and Wynn J. C. 1997. Geology of the Wabar meteorite craters (abstract #1313). 28th Lunar and Planetary Science Letters. CD-ROM.

Spencer L. J. and Hey M. H. 1933. Meteoritic iron and silica-glass from the meteorite craters of Henbury central Australia and Wabar Arabia. *Mineralogical Magazine* 23:387–404.

Stöffler D. and Langenhorst F. 1994. Shock metamorphism of quartz in nature and experiment: I. Basic observation and theory. *Meteoritics* 29:155–181.

Storzer D. and Wagner G. A. 1977. Fission track dating of meteorite impacts. *Meteoritics* 12:368–369.

Wynn J. C. 2002. Mapping an iron-meteorite impact site with a magnetometer, and implications for the probability of a catastrophic impact on Earth. *Journal of Environmental & Engineering Geophysics* 7:143–150.

Wynn J. C. and Shoemaker E. M. 1998. The day the sands caught fire. *Scientific American* 279:36–45.

Yang X., Zhang F., Fu X., and Wang X. 2008. Oxygen isotopic composition of quartz in the sand seas and sandy lands of northern China and their implications for understanding the provenances of aeolian sands. *Geomorphology* 102:278–285.

SUPPORTING INFORMATION

Additional supporting information may be found in the online version of this article:

Fig S1: X-ray diffractogram of the HF-treated shock-lithified sand WB08-4. The residuum shows the presence of abundant coesite (Cs), stishovite (Sts), zircon (Zrc), and tungsten carbide (WC) from the mill.

Fig S2: Cathodoluminescence images. Qtz = quartz; Ep = epoxy. a) Zoned, shattered quartz grains in sample WAHA1. The reddish color indicates sand grains of volcanic origin, whereas grains with darker color derived from plutonic or metamorphic rocks (probably from 11 m crater); b) Partially melted section in sample WAHA2. Dark blue quartz grains show light-colored rims (transformation into glass). Grains are surrounded by vesicle-rich lechatelierite. c) Section of sample WAHA2 where quartz has been transformed into a relatively homogeneous white-greenish quartz glass (lechatelierite). d) Black bomb (WAHA3) ejected from Philby-A or Philby-B crater. The dark rim to the left lacking luminescence is made of black impact glass. The colored right side is made of a white shock-lithified sand showing zoned quartz grains transforming to a quartz glass at the contact with the black impact glass.

Table S1: Carbon isotope data of *Cornulaca Arabica* stems.

Appendix S1: Locations of iron meteorite fragment recovery.

Appendix S2: Analytical methods.

Appendix S3: Radiocarbon data.